Monazite LaPO 4 :Eu 3+ nanorods as strongly polarized nano-emitters

Zijun Wang, Jeongmo Kim, Lilian Magermans, Francesca Corbella, Ileana Florea, Eric Larquet, Jongwook Kim, Thierry Gacoin

Monazite $LaPO_4:Eu^{3+}$ Nanorods as Strongly Polarized Nano-Emitters

Zijun Wang,[a] Jeongmo Kim,[a] Lilian Magermans,[a] Francesca Corbella,[a] Ileana Florea,[b] Eric Larquet,[a] Jongwook Kim*[a] and Thierry Gacoin*[a]

[a.] *Laboratoire de Physique de la Matière Condensée, Ecole Polytechnique, CNRS, IP Paris, 91128 Palaiseau, France.*
[b.] *Laboratoire de Physique des Interfaces et des Couches Minces, Ecole Polytechnique, CNRS, IP Paris, 91128 Palaiseau, France*

*E-mail: jong-wook.kim@polytechnique.edu
*E-mail: thierry.gacoin@polytechnique.edu

Orientation analyses of macromolecules or artificial particles are vital for both fundamental research and practical bio-applications. An accurate approach is monitoring the polarization spectroscopy of lanthanide-doped in nanocrystalline materials. However, nanomaterials are often far from ideal for the colloidal and polarization luminescence properties. In the present study, we synthesize well-dispersed $LaPO_4:Eu^{3+}$ nanomaterials in an anisotropic rod shape. Microwave heating with excess addition of phosphate precursor invokes a rapid phase transition of rhabdophane into monazite. The colloidal stability of the nanorod suspension is outstanding, demonstrated by showing liquid crystalline behaviors. The monazite nanorods are also superior in luminescence efficiency with limited defects. The emission spectrum of Eu^{3+} consists of well-defined lines with prominent polarization dependencies for both the forced electric dipole transitions and the magnetic dipole transitions. All the results demonstrate that the synthesized monazite nanorods can serve as an accurate probe in orientation analyses and potential applications, such as in microfluidics and biological detections.

Introduction

Retrieving orientational information of macromolecules or artificial labeling particles has captured growing attention in many fields, such as mechanobiology and microfluidics.[1,2] Determining the orientation on a small scale (order of nanometer) is usually based on the local measurement of anisotropic physical properties. Optical properties, such as polarized luminescence, are preferred as they can be measured using high-performance optical microscopies with high resolution and accuracy.[3,4] Probing species or labels are those having a defined orientation of emission dipoles. Single molecules are widely used but suffer from photobleaching.[1,5] Luminescent nanoparticles exhibiting down/upconversion, downshifting, and second-harmonic generation,[6-8] are interesting alternatives due to their robust structures and potentially excellent polarization effects in absorption (dichroism) and emission.

When crystallized in an anisotropic shape,[9-11] the polarization anisotropy linked to the crystalline axis correlates with the geometrical axis of the particle. A single luminescent nanoparticle provides an emitting dipole with a specific axis with respect to the geometrical axis. The anisotropic shape allows the orientation of particles by external fields, such as electric or magnetic fields,[12,13] and shear stress in a flowing liquid.[14,15] For instance, semiconductor quantum rods possess a single polarized optical transition governed by quantum confinement,[9,16-19] thus can be used for orientation analysis. More recently, attention has been paid to lanthanide-doped nanoparticles.[15,20,21] In this case, multiple emission lines are observed stemming from intra-configurational 4f-4f transitions. Their relative intensity is very sensitive to the local symmetry in the host crystal structure.[22,23] Interestingly, the localized emitting states from the activator ions are independent of particle size and shape and are polarized along the axis determined by the crystalline structure.[24] This opens up the use of lanthanide-doped particles for orientation analysis, and some reports on microcrystals are already interesting for applications, e.g. optical devices and biological sensors.[4,15,25-29] Our group recently reported an original methodology of orientation determination based on Eu^{3+} emission.[30] The orientation analysis can then be realized by collecting either two dipole emissions at a single polarization angle or one dipole emission at two polarization angles. This emphasizes the interest in using lanthanide-doped nanocrystals as labels for orientation determination at a single-particle level. One can also statistically determine an averaged degree of particle orientation and further local measurements of the amplitude of the external stimuli.[31]

Rhabdophane $LaPO_4$:Eu nanorods were found to be an excellent system to provide the proof of concept of orientation analysis using lanthanide-doped nanoparticles.[12,14] Synthesized under hydrothermal conditions, these particles exhibit outstanding colloidal properties. By using the rhabdophane nanorods oriented by flow-induced shear stress,[32,33] we demonstrated a completely new methodology for a flow shear tomography in microfluidic channels.[31] However, the low degree of polarization (DOP) in the forced electric dipole transition of rhabdophane $LaPO_4$:Eu has limited the resolution of orientation analysis and the measurement dimensions of flow shear tomography. Hence, we have investigated other candidate compounds exhibiting high DOPs in both forced electric and magnetic dipole transitions that are essential for precise three-dimensional (3D) orientation analysis. This led us to consider the polymorphs of $LaPO_4$ and evidence was found that $LaPO_4$ with the high-

temperature monazite phase exhibits largely improved polarized luminescence as compared to the rhabdophane $LaPO_4$.[23] In addition to an increased emission intensity, allowing for a better signal-to-noise ratio, the monazite phase shows significantly higher DOPs on multiple emission lines. This raises the possibility to perform a fully 3D flow shear tomography with high spatiotemporal resolution as two spherical angles of particle orientation can be simultaneously determined using both forced electric and magnetic dipoles.[30,31]

In the previous study, the polarization properties were characterized on monazite $LaPO_4$ microdomains via a high-temperature thermal treatment (>800 °C) of aligned rhabdophane nanorods.[23] The thermal treatment obviously leads to the loss of any possibility to recover a colloidal suspension. Our idea was thus to develop a colloidal synthesis method allowing for producing monazite $LaPO_4$ nanorods, rather than rhabdophane, maintaining the anisotropic morphology (nanorods in lengths of around 100 nm and aspect ratios of more than 10). Many examples are known in colloid chemistry on compounds in which polymorphic structures could be directed by playing on the synthesis conditions.[34-36] Regarding $LaPO_4$, previous works did report the formation of the monazite phase using solvothermal syntheses at temperatures above 200 °C.[37-42] However, poor attention was paid to the control of size and aggregation state for the final particles, which are of drastic importance for their applications. Our present study thus aims in revisiting the colloidal synthesis of $LaPO_4$ targeting nanoparticles with optimized crystal structure, morphology, and colloidal stability at the same time. We here demonstrate that under optimized synthesis conditions, playing on microwave heating and precursor stoichiometry, it is possible to boost the phase transition from rhabdophane to monazite while preserving the rod shape of particles with a high aspect ratio. The obtained monazite nanorods present excellent colloidal dispersion properties and thus show liquid crystalline behaviors. Doped with Eu^{3+} ions, these nanorods show intense and highly polarized emission lines, evidencing a crystalline quality similar to that for the annealed sample.[23] This study opens the way for using monazite $LaPO_4$ nanorods as outstanding labels for orientation tracking and shear flow analysis.

Experimental

Chemicals The synthesis was conducted using commercially available reagents. Lanthanum (III) nitrate hexahydrate ($La(NO_3)_3{\cdot}6H_2O$, 99.99%), lanthanum (III) oxide (La_2O_3, 99.9%), europium (III) nitrate pentahydrate ($Eu(NO_3)_3{\cdot}5H_2O$, 99.9%), europium (III) oxide (Eu_2O_3, 99.9%), di-ammonium phosphate ($(NH_4)_2HPO_4$, Analytical Reagent, A.R.), ethylene glycol (A.R.) and nitric acid (HNO_3, 70%, A.R.) were purchased from Sigma-Aldrich and used without further purification.

Synthesis of monazite $LaPO_4$:5%Eu^{3+} nanorods with excess phosphate Aqueous solutions of 0.05 M $La(NO_3)_3$, $Eu(NO_3)_3$ in total 10 mL, and 12 mL $(NH_4)_2HPO_4$ (20% excess) were mixed in a microwave glass tube. Except for specific experiments, a doping concentration of 5% was used all through this work. The mixture with an initial pH value of 2 was heated in a microwave reactor (Discover SP, CEM) at 160 °C for 2 h. After cooling down, the products were collected by centrifugation at 8000g for 20 min and then dispersed in pH=2 water (HNO_3). The suspension was then dialyzed (12-14 kDa) against pH=2 water (HNO_3) for two days and then sonicated. The powder samples for characterizations were obtained by drying the final suspension at 100 °C overnight. To investigate the concentration quenching, Eu^{3+} concentration was varied from 0.5 to 100% in molar ratio. The obtained samples in powder form were subsequently heated to 1000 °C for 1 h.

Synthesis of monazite $LaPO_4$:5%Eu^{3+} nanorods with excess acid All parameters in the reaction were the same, except that stoichiometric amounts of precursors were used, dissolved in 0.4 M HNO_3 water.

Suspension in ethylene glycol Dialyzed nanorod suspension was transferred into ethylene glycol to concentrate the nanorods. After adding ethylene glycol into the aqueous suspension, the water was removed by using a rotary evaporator. The suspension was then dialyzed (12-14 kDa) against pure ethylene glycol for one week.

Synthesis of bulk $LaPO_4$:5%Eu^{3+} powders Microcrystalline $LaPO_4$ doped with 5% europium was synthesized by the solid-state method. Lanthanide oxide and diammonium phosphate in stoichiometric amounts were mixed and ground together in an agate mortar with subsequent heating at 800 °C for 1 h. The mixture was ground and heated again at 1100 °C for 12 h.

Characterizations Powder X-ray diffraction (XRD) measurements were performed on a Bruker D8 Advance diffractometer at Cu Kα radiation (λ=1.5409 Å) with a LynxEye XE-T detector. Scanning electron microscopy (SEM) images were obtained on a Hitachi S4800 microscope with a field emission electron gun at 5 kV. High-resolution transmission electron microscopy (HR-TEM) was performed on an FEI Titan Themis microscope operating at 300 kV with a Falcon III camera of direct electron detector. STEM mode was operated on a probe Cs corrected FEI Titan Themis microscope at 200 kV, equipped with a Super-X 4-dial detection system for Energy Dispersive X-ray analysis (EDX). For the sample preparation, the diluted colloidal suspension was dropped on the ultrathin carbon-coated (3 nm) copper grids. Zeta potential and dynamic light scattering (DLS) were measured by a Malvern ZetaSizer Nano ZS. High-temperature anneal was performed in a Nabertherm furnace.

Birefringence images were collected on a conventional polarizing optical microscope (Olympus BX51WI). Liquid crystalline nanorods on a slide in front of a fixed polarizer were illuminated by a white-light halogen bulb (100 W). The transmitted light through the sample was collected with an objective (10×, NA=0.3). After a rotating thin film polarizer, a CCD camera (Discovery DTA 1600E) was used to capture the image.

Emission and excitation spectra were measured on a commercial spectrofluorometer (FluoroMax-4p, Horiba) with a 150 W xenon lamp and a Hamamatsu R928P photomultiplier tube. Photoluminescence decay curves were measured with a µs-flash lamp at a repetition rate of 20 Hz. Samples were in powder form to have a better comparison of emission intensities than on colloidal suspensions for which different scattering properties may be misleading. Polarized luminescence measurements were performed using a confocal optical microscope (Nikon TI-DH) at room temperature. A continuous-wave mode fiber-coupled 394 nm diode laser (OXXIUS) was used as the excitation source. After collimation, the excitation beam was circularly polarized through a quarter waveplate and then reflected by a long-pass dichroic mirror to focus on the sample through an objective (100×, numerical aperture NA=0.9). The emission light of the sample went through the same objective and then was focused on a 50 µm pinhole. After collimation and phase shift by a half waveplate, the beam was reflected by a polarizing beam-splitter to enable the selected polarization of light parallel along the slit. Subsequently, the beam was focused on a spectrometer (IsoPlane SCT-320, Teledyne Princeton Instruments) and detected by a charge-coupled device (CCD, PIXIS 400, Teledyne Princeton Instruments).

Results and discussion

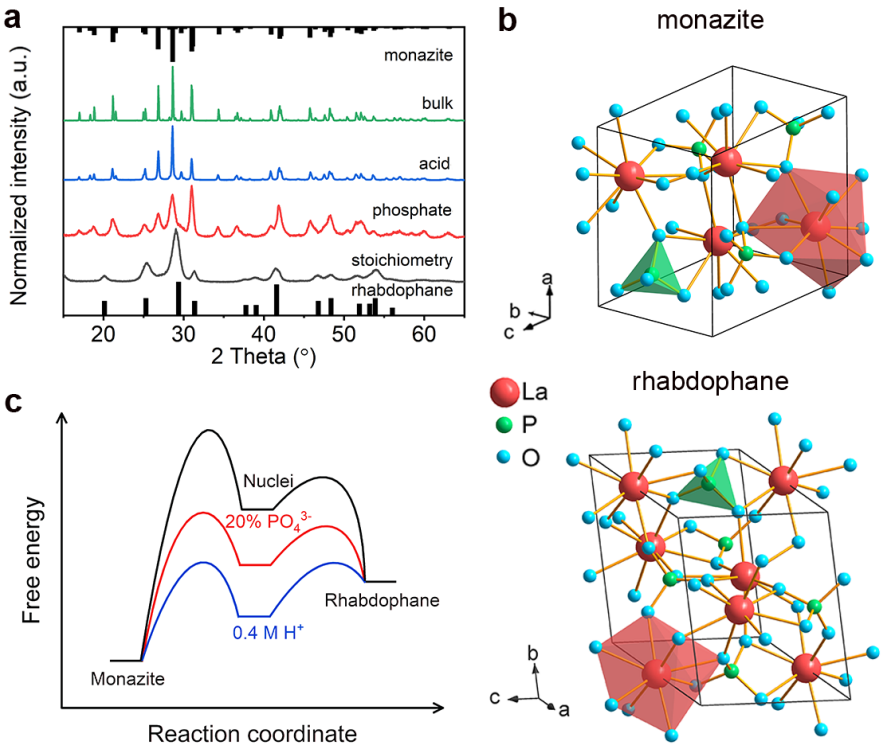

Figure 1. Phase evolution of the monazite $LaPO_4$:5%Eu^{3+} synthesized in the presence of excess acid and phosphate under microwave heating at 160 °C. (a) XRD patterns in different synthesis parameters and reference diffraction lines (rhabdophane: JCPDS 04-0635; monazite: JCPDS 84-0600). (b) Illustration of the crystallographic structures in a unit cell showing the coordination and polyhedra around the La and P atoms, respectively. (c) Schematic illustration of the free energy landscape for the rhabdophane and the monazite phases under our experimental conditions.

Chemical monitoring of the polymorphic structure Crystal structures of the compounds obtained in different synthesis conditions were characterized by XRD measurements as shown in **Figure 1a**. Consistently with our previous work,[12] the sample obtained with a stoichiometric ratio of lanthanide and phosphate precursors (initial pH of 2) exhibits an XRD pattern well ascribed to the rhabdophane phase, a hexagonal structure shown in **Figure 1b**. Starting from this synthesis, the formation of another polymorph could be feasible by tuning different parameters, e.g. reaction temperature, pH of precursor solutions, and relative ratio of precursors.[34-36] The latter strategy has been successfully applied in some other systems, such as $NaYF_4$,[43] $BiPO_4$,[44] and YPO_4.[45]

In our case, the reaction temperature was set relatively low (160 °C) in order to limit irreversible aggregation and crystal growth as well dispersed nanorods with a relatively small size (100 nm) are targeted. After preliminary experiments, we found that producing monazite $LaPO_4$ (structure shown in **Figure 1b**) can be realized by the addition of either 20% excess $(NH_4)_2HPO_4$ or 0.4 M nitric acid in the mother solution. At that step, a difference between the two syntheses is only seen in the shape of the diffraction lines. Broad diffraction peaks for the phosphate-excess synthesis indicate nanocrystalline particles. In contrast, sharp and well-defined diffraction peaks are observed in the case of acid-excess synthesis, evidencing microcrystalline monazite particles. This is similar to the bulk material, synthesized by solid-state reaction.[46]

Mechanism of polymorph formation At this step, a question is raised about the mechanism of crystal phase transition through the simple addition of excess phosphate or acid keeping a relatively low-temperature microwave synthesis. Understanding how the crystal grows and evolves benefits an elaborate control on the phase and shape of the particle while preserving the dispersion quality of the colloidal solution. Information is obtained through analyzing aliquots of the samples after different aging times under microwave heating (still at 160 °C). **Figure S1** shows XRD patterns of collected precipitates either instantly after mixing the precursors at ambient temperature or after only 5 min of microwave reaction at 160°C. In the case of the phosphate-excess synthesis, the formation of the rhabdophane phase occurs immediately once the reactants are mixed. A subsequent microwave heating instantly triggers a phase transition into the monazite structure. A different evolution is observed in the case of the acid-excess synthesis, and the visual aspect of the reaction mixture is shown in **Figure S2** before and after the microwave synthesis. After mixing the precursors, the mixture is fully transparent and homogeneous, evidencing a significant solubility of the rhabdophane phase in strongly acidic media (0.4 M HCl). It is the following treatment by microwave heating that rapidly induces the formation of particles that directly exhibit the monazite structure.

To further understand the role of the excess phosphate and acidity in the phase transition, pre-formed rhabdophane particles (obtained using a stoichiometric ratio of precursors) were reacted with either 0.4 M acid or 20% excess phosphate. Monazite particles were collected after microwave treatment when the 0.4 M acid was added whether the original rhabdophane particles had been washed or not. In contrast, only the unwashed rhabdophane solution further reacted with 20% excess phosphate results in the monazite phase. We thus conclude on the active role of counter-ions for the phase transformation.

Based on these observations, a dissolution-recrystallization mechanism can be inferred for the phase transition. Two parameters should be considered. One is the equilibrium constant for the transformation of one phase (dissolved precursors, monazite, or rhabdophane phases) to another, as determined by the difference of free energies of the considered phases.[43,44] The second one is the activation energy that determines the reaction kinetics of dissolution/precipitation for each of the two solid phases.

All our observations show that the precipitation into the rhabdophane phase is kinetically favored, as seen by its formation in pH=2 water. However, this phase is completely soluble in a very acidic medium (0.4 M HCl) meaning that the free energy of the corresponding precursor solution is lower in this case than the one of the rhabdophane phase. Now considering the monazite phase, it appears as thermodynamically more stable than the rhabdophane phase since upon providing enough energy in the presence of excess acid and phosphate, only the monazite is obtained. Nevertheless, it only forms upon heating the precursor solution, which means that the activation energy for the formation of this phase is much higher than the one required to form the rhabdophane phase. All these observations, described by the free energy landscape schematically shown in **Figure 1c**, fit well with a monazite structure formation occurring through a thermally induced dissolution/reprecipitation process, considering that dissolution does not have to occur in strongly acidic media where the rhabdophane phase is soluble at ambient temperature.

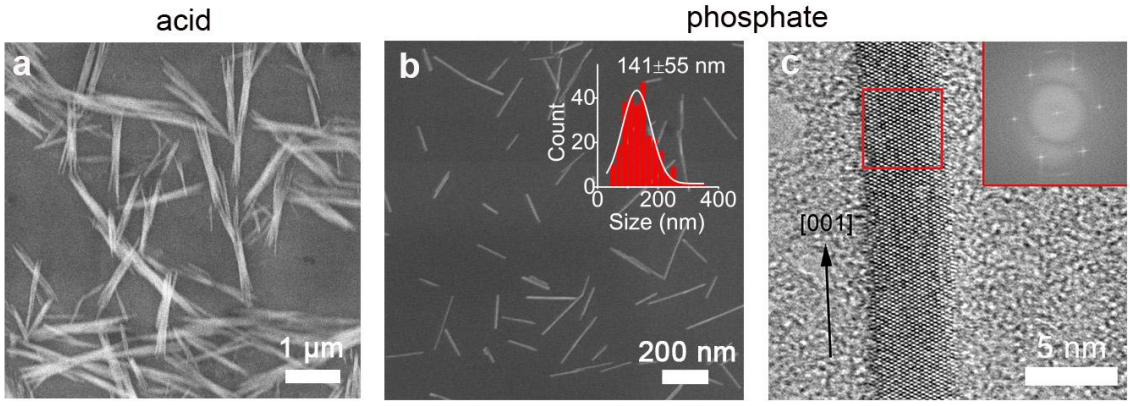

Figure 2. Electron microscopy characterizations for the monazite $LaPO_4$:5%Eu^{3+} nanorods synthesized in the presence of (a) 0.4 M acid and (b, c) 20% excess phosphate. (a, b) SEM images and histograms of length distribution. (c) HR-TEM image and FFT as

an inset.

Nanocrystal morphology and crystallinity Morphology and size of particles were characterized by electron microscopy on samples made by drop-casting from purified suspensions. **Figure 2a** shows that in the condition of excess acid nanoparticles appear as bundles of nanorods, in which the large size is in good agreement with the high coherence length expected from the narrow diffraction peaks in **Figure 1a**. High ionic strength may explain the agglomeration into bundles. In contrast, for the monazite nanorods synthesized with excess phosphate (**Figure 2b**), individual nanorods are seen with a mean length of 141±55 nm and an aspect ratio of 28±11 (a mean width of 6±1 nm). Compared with the rhabdophane nanorods (a mean length of 144±56 nm and an aspect ratio of 27±13, **Figure S3**) synthesized with stoichiometric precursors and other identical parameters, the excess phosphate does not significantly influence the particle shape and length.

Further, structural characterizations were achieved using HR-TEM. The image in **Figure 2c** reveals good mono-crystallinity for a single monazite nanorod, demonstrated by the periodic fringe patterns of lattice planes and the clear electron diffraction patterns in the fast-Fourier transform (FFT) analysis. The high-angle annular dark-field imaging on a STEM mode (**Figure S4**) reveals the crystal growth along the c axis, which is consistent with the anisotropy in the monoclinic crystallographic structure of $LaPO_4$.[39,47] EDX analysis (**Figure S5, S6**) confirms a homogeneous distribution of Eu dopants along the nanorods and the Eu content is close to the nominal one.

Colloidal stability Regarding the potential applications, an important issue is to get individualized particles perfectly dispersed as a colloidal suspension. A systematic study led us to select 160 °C as an optimal temperature of synthesis and a precursor concentration of 0.05 M (details in **Supplementary Information** with **Figure S7-9**). These conditions were found to ensure a good crystallization of the monazite phase while preserving an excellent particle dispersion.

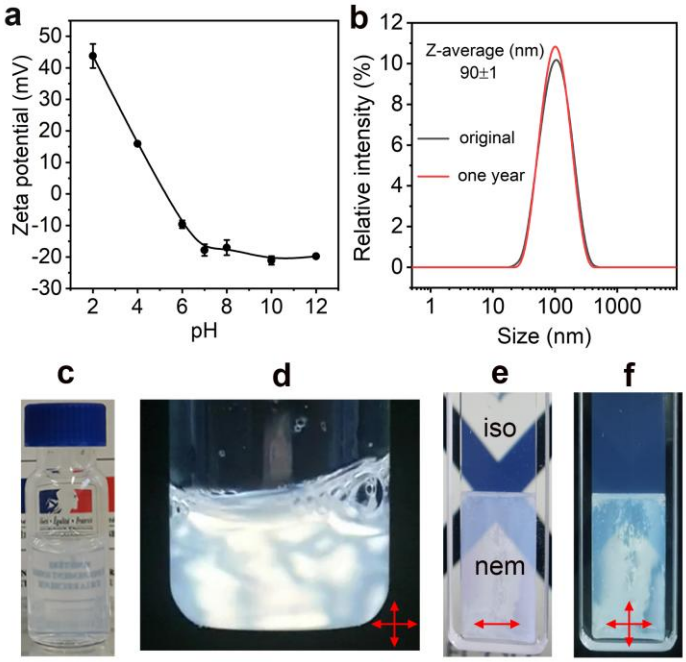

Figure 3. Colloidal stability for the monazite $LaPO_4$:5%Eu^{3+} nanorods synthesized with excess phosphate. (a) Zeta potential as a function of pH value. (b) Hydrodynamic diameter of nanorod measured by DLS in the aqueous suspension (fresh and one year later) labeled with Z-average size. (c) An image of aqueous nanorod suspension (Φ=0.4% and pH=2). (d) Corresponding flow birefringence under crossed polarizers. (e) Macroscopic isotropic liquid-nematic (iso-nem) phase separation of nanorod suspension in ethylene glycol (original Φ=5%) in a 2 mm-think quartz cell. (f) Corresponding birefringence for the bottom nematic phase under crossed polarizers. Note that the significant light scattering shown in (d-f) is due to scattering from birefringent nematic domains observed under cross polarizers (d,f).

After the synthesis, the nanorods were dialyzed against pH=2 water to remove excess ions thus reducing ionic strength to ensure efficient electrostatic repulsion. The choice for pH=2 is justified by the zeta potential measurements (**Figure 3a**), which also confirm the point of zero charge at pH=5.3 that is consistent with previous report.[48] From that point, zeta potential remains at around -20 mV toward alkaline environments, while it is as high as 44±4 mV in the acidic media at pH=2. This strong positive electrostatic charge is expected to result from surface La^{3+} ions and protonated phosphates. Benefited from the dialysis,

the obtained suspension exhibits excellent colloidal stability for more than one year at a relatively high concentration of nanorod (volume fraction/Φ=0.4% and 20 g/L). The good nanorod dispersion without aggregates is demonstrated by the DLS measured small size (**Figure 3b**), the optical transparency of the suspension (**Figure 3c**), and the SEM image (**Figure 2b**) showing well-dispersed particles.

Considering the remarkable colloidal stability and the well-controlled anisotropic particle shape and size, the monazite $LaPO_4$:5%Eu^{3+} nanorods synthesized with excess phosphate are expected to orient under flow shear stress.[14,15] Orientation of nanorods can be examined by birefringence under crossed polarizers.[49,50] In the aqueous suspension (pH=2 and Φ=0.1%) under a static state, the nanorods are randomly orientated. When a flow is generated by simple shaking of the solution as displayed in the **Supplementary Information** video, clear flow birefringence can be observed as the flow shear stress instantly aligns the nanorods along the direction of shear. The nanorods progressively return to their averaged random orientation once the flow stops. A captured frame in the video (**Figure 3d**) shows a typical texture of flow birefringence, evidencing a local variation of nanorod orientation.

Investigation of suspension with an extremely high-volume fraction (Φ=5%, i.e. 250 g/L) can be achieved by transferring the particles into ethylene glycol, a medium that provides outstanding colloidal stabilization by both electrostatic repulsion and steric hindrance.[12] As shown in **Figure 3e**, macroscopic phase separation can occur within one day, characteristic of the isotropic to the nematic transition, driven by the liquid crystalline self-assembly of the nanorods. Highly birefringent nematic domains can be observed under crossed polarizers (**Figure 3f**). Such a phase separation, observed for the first time on monazite nanorods, is additional evidence of the excellent quality of the dispersion even at very high concentrations. Additionally, the phase separation realizes a size filtering as shown in **Figure S10**, nanorods being shorter in the isotropic phase than in the nematic phase. This size filtering allows for an improvement of the size distribution of the rods, which will benefit the sensitivity and accuracy of orientation analysis in microfluidics.[31]

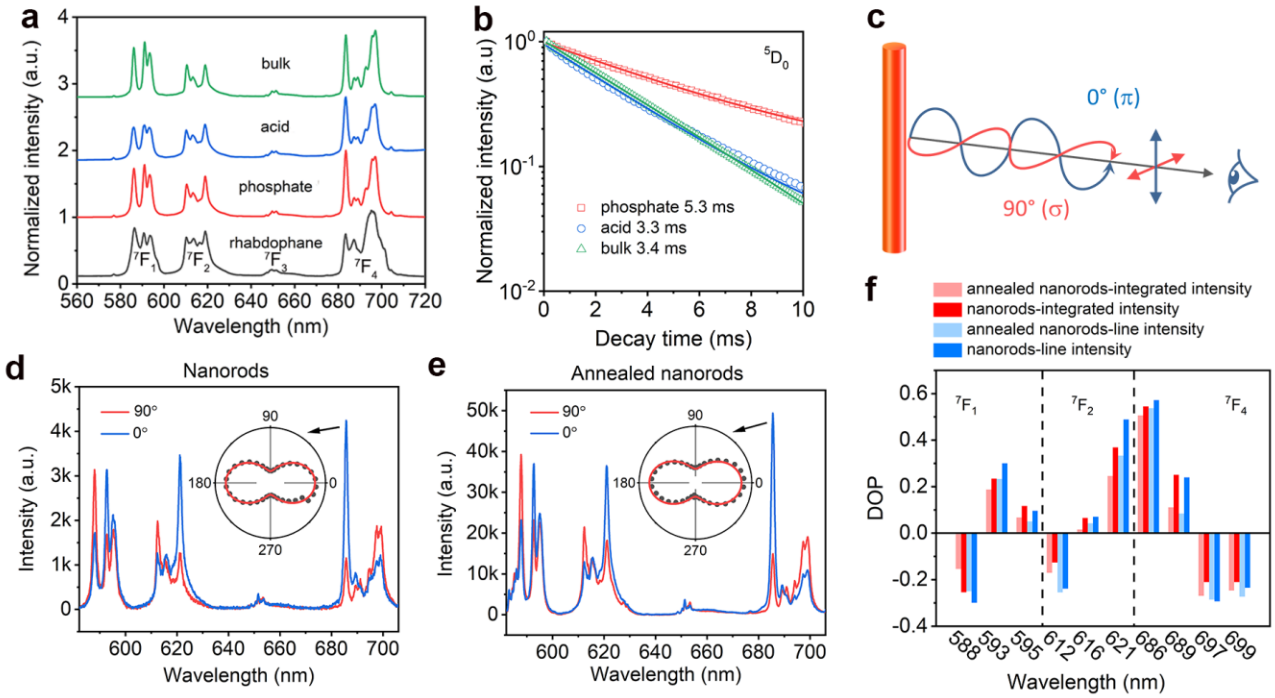

Figure 4. Luminescence properties for the monazite nanorods synthesized with excess phosphate. (a) Emission spectra under 394 nm $^5L_6$ excitation labeled by the final states for the emission from the $^5D_0$ state for the rhabdophane nanorods, monazite nanorods in the presence of excess phosphate or acid, and bulk material. (b) Luminescence decay curves of $^5D_0$ emission under 394 nm excitation for monazite nanoparticles and bulk material. (c) Schematic illustration of emission observation from aligned nanorods by changing analyzer from 0° to 90° (parallel and perpendicular to the orientation of nanorod). Polarized luminescence of (d) nematic aligned nanorods in comparison with (e) aligned nanorod film after annealing. Insets are polar diagrams and fitting curves for the integrated intensity of the 686 nm emission line. (f) Calculated DOPs for each emission line derived from the polarized emission spectra (d, e) for the nanorods (dark-color bars) and annealed nanorods (light-color bars). Red and blue represent the calculation by integrated intensity area in specific wavelength ranges and maximum line intensity, respectively.

Luminescence property Figure 4a shows the normalized emission spectra under 394 nm excitation for the different $LaPO_4$:5%Eu^{3+} samples in this study (monazite synthesized with excess phosphate or acid, rhabdophane, and bulk monazite material). The observed spectra are in full agreement with those previously reported for the monazite and rhabdophane phases,[23] confirming their spectroscopic specificity to the crystal phases as deduced from XRD measurements (**Figure 1a**). The excitation spectrum (**Figure S11**) shows characteristic Eu^{3+} excitation lines with an intense line at 394 nm due to the $^7F_0$-$^5L_6$ transition. Fast relaxation to the $^5D_0$ state is followed by radiative decay through $^5D_0$-^7F_J (J=1, 2, 3, 4) transitions, which are split into various components by crystal field. One can distinguish the forced electric dipole transitions ($^5D_0$-$^7F_2$ at 612, 615, and 620 nm, $^5D_0$-$^7F_3$ at 646-653 nm, and $^5D_0$-$^7F_4$ at 681-706 nm) and the magnetic dipole transitions ($^5D_0$-$^7F_1$ at 587, 592, and 595 nm). The emission spectrum for the monazite nanorods is identical to that for the bulk material in terms of line width and line position. This is a good indication of the excellent crystallinity of the nanorods.

To optimize the brightness of these monazite particles, an investigation was made regarding the optimal Eu^{3+} concentration, an issue raised by the concentration quenching effect well known in phosphors.[51] We nevertheless found that our microwave synthesis cannot produce pure monazite particles for Eu^{3+} concentration higher than 20-40% (120-200 °C) depending on the heating temperature, probably because the size of the substitutional ion impacts the polymorph stability, similarly to what has been largely investigated in $NaYF_4$ compounds.[52,53] As an example, XRD patterns are shown in Figure S12 for the samples under the heating temperature of 200 °C. When the Eu^{3+} concentration is more than 40%, there is a transition from monazite to rhabdophane phase. The concentration-dependent study is thus achieved on samples that have been annealed at 1000 °C for 1h to ensure a complete phase transition to monazite phase. As shown in **Figure S13**, the highest emission intensity is obtained for Eu^{3+} concentration of about 50%. In comparison, the emission intensity for the 5% doping sample is about four times less. Nevertheless, the unannealed monazite nanoparticle at this doping concentration is still about 3-fold more intense than the rhabdophane nanoparticles, indicating an enhanced quantum efficiency after the phase transition.[54]

To further provide an insight into the quantum efficiency and possible defects, $^5D_0$ decay dynamics (**Figure 4b**) was studied for the different monazite samples. All the decay curves exhibit a mono-exponential behavior. The excess phosphate synthesized monazite nanorods are longer in lifetime than the bulk material (5.3 vs 3.4 ms) due to the dielectric effect (an increase of radiative lifetime due to a lower effective refractive index).[55,56] Based on the radiative lifetime for Eu^{3+} in bulk material (assuming 100% quantum yield), quantum yield of Eu^{3+} emission can be quantitatively determined for the two species of nanoparticles.[46,57] The corresponding quantum yield is 28% and 18% for the excess phosphate and acid synthesized nanorods, respectively. Annealing of the excess phosphate synthesized nanorods at 1000 °C for 1 h (**Figure S14**) maintains the lifetime at 5.3 ms, whereas the lifetime is lengthened from 3.3 to 4.3 ms for the excess acid synthesized monazite. This is clear evidence for the excellent crystallinity of the nanorods with limited defects synthesized with excess phosphate. The excess acid synthesized particles are not the case, although with a larger size and even after high-temperature annealing.

Polarized luminescence We now discuss polarization features of the emission, the property that is directly taken into consideration for the targeted application of orientation tracking. Changing the angle of a polarization analyzer with respect to the nanorod axis leads to a variation of the relative intensity of the different components in the emission spectra.[26] Characterization of polarization should be done on either oriented assembly of particles[15,23] or a single particle.[26,28,58] In this work, experiments were made on the nematic phase of excess phosphate synthesized nanorods as the order parameter of nanorods is expected to be near 1.[21,59] The nematic domain was localized and visualized in a confocal microscope. Under crossed polarizers, clear birefringence texture was observed (**Figure S15**). The nematic ensemble of nanorods emitted sufficient light intensity for analysis with a high signal-to-noise ratio as compared with measurements on single particles.

The emission light is produced under excitation at 394 nm. A polarizer is put in front of the spectrometer detecting the emitting photons. When the polarizer is parallel (0°) and perpendicular (90°) to the axis of the nanorod, π and σ spectra are collected, respectively (**Figure 4c**). **Figure 4d, e** compares the π and σ spectra for the monazite nanorods in this work and the annealed nanorod film in our previous work,[23] in which the nanorods are aligned by blade coating.[14] Note that for comparison, the spectra must be collected under the same conditions. The crystal field split components alter the relative intensity upon changing the analyzer angle. The two samples show similar polarized emission spectra. Each polarized emission line also shows a similar polar diagram as a function of the analyzer angle. As an example, the polar diagrams are plotted for the integrated intensity of the 686 nm emission line as the insets in **Figure 4d, e**. For quantitative analysis, the magnitude of emission polarization can be characterized by a degree of polarization (DOP), defined by $(I_{0°}-I_{90°})/(I_{0°}+I_{90°})$, where $I_{0°}$ and $I_{90°}$ denote the luminescence intensity with polarizer parallel and perpendicular to the nanorod orientation. DOPs are compared for the two samples in **Figure 4f**, integrating the spectra in wavelength ranges corresponding to the main emission lines (**Figure S16**). Another representation is given in **Figure S17**, presenting DOP at all wavelengths directly making the calculation using the full π and σ emission spectra. Both samples (monazite nanorods from this work and the annealed nanorod film from ref. 23) exhibit very similar polarization features for both the forced electric dipole and magnetic dipole transitions. Their DOPs are close and are especially high (~0.55) for the 686 nm $^5D_0$-$^7F_4$ transition line. These results confirm that monazite $LaPO_4$ is a superior matrix in realizing Eu^{3+} polarization properties and demonstrate the successful production of nanorods with preserved properties similar to the bulk references.

Conclusions

In summary, we have synthesized monazite $LaPO_4$:5%Eu^{3+} nanorods under mild hydrothermal conditions using microwave heating. As compared to the previously reported synthesis on rhabdophane nanorods, we have shown that additional 20% phosphate with optimized experimental parameters invokes the phase transition to monazite while preserving the rod shape of the particles. Suspensions of these nanorods exhibit outstanding colloidal stability and can be concentrated up to a point where characteristic liquid crystalline behavior emerges as proof of excellent colloidal quality. Remarkably, optimized nanorods exhibit a high crystallinity without a significant amount of defects, leading to emission properties similar to the bulk compounds. The polarization measurements of Eu^{3+} emission reveal high DOPs for both the forced electric dipole and the magnetic dipole transitions, confirming our previous work achieved on microdomains of aligned nanorods. Based on the high quantum efficiency, high DOPs in multiple emission lines, and the excellent dispersion, the present nanorods are outstanding candidates used as high-resolution probes in 3D orientation analysis and for pursuing the investigation to use such colloidal probes for the 3D tomography of flow shear stress in microfluidics and biofluids.

ORCID

Zijun Wang: 0000-0001-8937-2975
Jongwook Kim: 0000-0003-0404-6973
Thierry Gacoin: 0000-0001-6774-3181

Conflicts of interest

There are no conflicts to declare.

Acknowledgments

We thank to Gilles Patriarche for his help on the HAADF-STEM and EDX measurements and Éric Ngo for discussion. This research was supported by the Fondation pour la Recherche Médicale (DCM20181039556, programme Chimie pour la Médecine) and the French national research agency (ANR-19-CE09-0033, ANR-10-EQPX-0050).

References

1. D. Y. Shroder, L. G. Lippert and Y. E. Goldman, *Methods Appl. Fluoresc.*, 2016, **4**, 042004.
2. D. Kumar, A. Shenoy, S. Li and C. M. Schroeder, *Phys. Rev. Fluids*, 2019, **4**, 114203.
3. P. D. Cunningham, J. B. Souza, I. Fedin, C. She, B. Lee and D. V. Talapin, *ACS Nano*, 2016, **10**, 5769-5781.
4. P. Rodríguez-Sevilla, Y. Zhang, N. de Sousa, M. I. Marqués, F. Sanz-Rodríguez, D. Jaque, X. Liu and P. Haro-González, *Nano Lett.*, 2016, **16**, 8005-8014.
5. B. Kozankiewicz and M. Orrit, *Chem. Soc. Rev.*, 2014, **43**, 1029-1043.
6. S. Brasselet, V. Le Floc'h, F. Treussart, J.-F. Roch, J. Zyss, E. Botzung-Appert and A. Ibanez, *Phys. Rev. Lett.*, 2004, **92**, 207401.
7. L. Le Xuan, C. Zhou, A. Slablab, D. Chauvat, C. Tard, S. Perruchas, T. Gacoin, P. Villeval and J. F. Roch, *Small*, 2008, **4**, 1332-1336.
8. L. Mayer, A. Slablab, G. Dantelle, V. Jacques, A.-M. Lepagnol-Bestel, S. Perruchas, P. Spinicelli, A. Thomas, D. Chauvat and M. Simonneau, *Nanoscale*, 2013, **5**, 8466-8471.
9. Y. W. Jun, J. S. Choi and J. Cheon, *Angew. Chem. Int. Ed.*, 2006, **45**, 3414-3439.
10. Y. Fang, A. Xu, R. Song, H. Zhang, L. You, J. Yu and H. Liu, *J. Am. Chem. Soc.*, 2003, **125**, 16025-16034.
11. N. D. Burrows, A. M. Vartanian, N. S. Abadeer, E. M. Grzincic, L. M. Jacob, W. N. Lin, J. Li, J. M. Dennison, J. G. Hinman and C. J. Murphy, *J. Phys. Chem. Lett.*, 2016, **7**, 632-641.
12. J. Kim, A. de la Cotte, R. Deloncle, S. Archambeau, C. Biver, J. P. Cano, K. Lahlil, J. P. Boilot, E. Grelet and T. Gacoin, *Adv. Funct. Mater.*, 2012, **22**, 4949-4956.
13. H. Mundoor and I. I. Smalyukh, *Small*, 2015, **11**, 5572-5580.
14. J. Kim, J. Peretti, K. Lahlil, J. P. Boilot and T. Gacoin, *Adv. Mater.*, 2013, **25**, 3295-3300.
15. S. Shi, L. Sun, Y. Xue, H. Dong, K. Wu, S. Guo, B. Wu and C. Yan, *Nano Lett.*, 2018, **18**, 2964-2969.
16. D. V. Talapin, E. V. Shevchenko, C. B. Murray, A. Kornowski, S. Forster and H. Weller, *J. Am. Chem. Soc.*, 2004, **126**, 12984-12988.
17. M. Ohmachi, Y. Komori, A. H. Iwane, F. Fujii, T. Jin and T. Yanagida, *Proc. Natl. Acad. Sci.*, 2012, **109**, 5294-5298.
18. K. Thorkelsson, P. Bai and T. Xu, *Nano Today*, 2015, **10**, 48-66.
19. L. Yang, Z. Zhou, J. Song and X. Chen, *Chem. Soc. Rev.*, 2019, **48**, 5140-5176.
20. Y. Xie, Y. Li, G. Wei, Q. Liu, H. Mundoor, Z. Chen and I. I. Smalyukh, *Nanoscale*, 2018, **10**, 4218-4227.
21. H. He, J. Liu, K. Li, Z. Yin, J. Wang, D. Luo and Y. Liu, *Nano Lett.*, 2020, **20**, 4204-4210.
22. Y. Liu, D. Tu, H. Zhu and X. Chen, *Chem. Soc. Rev.*, 2013, **42**, 6924-6958.
23. E. Chaudan, J. Kim, S. Tusseau-Nenez, P. Goldner, O. L. Malta, J. Peretti and T. Gacoin, *J. Am. Chem. Soc.*, 2018, **140**, 9512-

9517.
24. K. Binnemans, *Coordin. Chem. Rev.*, 2015, **295**, 1-45.
25. J. Zhou, G. Chen, E. Wu, G. Bi, B. Wu, Y. Teng, S. Zhou and J. Qiu, *Nano Lett.*, 2013, **13**, 2241-2246.
26. P. Chen, M. Song, E. Wu, B. Wu, J. Zhou, H. Zeng, X. Liu and J. Qiu, *Nanoscale*, 2015, **7**, 6462-6466.
27. P. Rodriguez-Sevilla, L. Labrador-Paez, D. Wawrzynczyk, M. Nyk, M. Samoc, A. K. Kar, M. D. Mackenzie, L. Paterson, D. Jaque and P. Haro-Gonzalez, *Nanoscale*, 2016, **8**, 300-308.
28. D. Yang, Z. Peng, Q. Zhan, X. Huang, X. Peng, X. Guo, G. Dong and J. Qiu, *Small*, 2019, **15**, 1904298.
29. X. Yang, X. Lin, Y. Zhao, Y. Zhao and D. Yan, *Angew. Chem. Int. Ed.*, 2017, **56**, 7853-7857.
30. J. Kim, R. Chacón, Z. Wang, E. Larquet, K. Lahlil, A. Leray, G. Colas-des-Francs, J. Kim and T. Gacoin, *Nat. Commun.*, 2021, **12**, 1943.
31. J. Kim, S. Michelin, M. Hilbers, L. Martinelli, E. Chaudan, G. Amselem, E. Fradet, J. P. Boilot, A. M. Brouwer, C. N. Baroud, J. Peretti and T. Gacoin, *Nat. Nanotechnol.*, 2017, **12**, 914-919.
32. R. Cerf and H. A. Scheraga, *Chem. Rev.*, 1952, **51**, 185-261.
33. F. P. Bretherton, *J. Fluid Mech.*, 1962, **14**, 284-304.
34. X. Teng, Y. Zhu, W. Wei, S. Wang, J. Huang, R. Naccache, W. Hu, A. L. Y. Tok, Y. Han, Q. Zhang, Q. Fan, W. Huang, J. A. Capobianco and L. Huang, *J. Am. Chem. Soc.*, 2012, **134**, 8340-8343.
35. J. Han, Y. Huang, X. Wu, C. Wu, W. Wei, B. Peng, W. Huang and J. B. Goodenough, *Adv. Mater.*, 2006, **18**, 2145-2148.
36. H. Zhu, Y. Lan, X. Gao, S. P. Ringer, Z. Zheng, D. Song and J. Zhao, *J. Am. Chem. Soc.*, 2005, **127**, 6730-6736.
37. K. Riwotzki, H. Meyssamy, H. Schnablegger, A. Kornowski and M. Haase, *Angew. Chem. Int. Ed.*, 2001, **40**, 573-576.
38. K. Kompe, H. Borchert, J. Storz, A. Lobo, S. Adam, T. Moller and M. Haase, *Angew. Chem. Int. Ed.*, 2003, **42**, 5513-5516.
39. Y. Zhang, Z. Yan, L. You, R. Si and C. Yan, *Eur. J. Inorg. Chem.*, 2003, **2003**, 4099-4104.
40. O. Lehmann, K. Kompe and M. Haase, *J. Am. Chem. Soc.*, 2004, **126**, 14935-14942.
41. K. Riwotzki, H. Meyssamy, A. Kornowski and M. Haase, *J. Phys. Chem. B*, 2000, **104**, 2824-2828.
42. H. Meyssamy, K. Riwotzki, A. Kornowski, S. Naused and M. Haase, *Adv. Mater.*, 1999, **11**, 840-844.
43. H. Mai, Y. Zhang, R. Si, Z. Yan, L. Sun, L. You and C. Yan, *J. Am. Chem. Soc.*, 2006, **128**, 6426-6436.
44. P. Li, T. Yuan, F. Li and Y. Zhang, *J. Phys. Chem. C*, 2019, **123**, 4424-4432.
45. P. Li, Y. Zhang, L. Zhang, F. Li, Y. Guo, Y. Li and W. Gao, *Cryst. Growth&Des.*, 2017, **17**, 5935-5944.
46. J. J. H. A. van Hest, G. A. Blab, H. C. Gerritsen, C. D. Donega and A. Meijerink, *J. Phys. Chem. C*, 2017, **121**, 19373-19382.
47. N. Clavier, R. Podor and N. Dacheux, *J. Eur. Ceram. Soc.*, 2011, **31**, 941-976.
48. T.-W. Cheng, P. Holtham and T. Tran, *Miner. Eng.*, 1993, **6**, 341-351.
49. P. Davidson and J.-C. P. Gabriel, *Curr. Opin. Colloid Interface Sci.*, 2005, **9**, 377-383.
50. J. C. Gabriel and P. Davidson, *Adv. Mater.*, 2000, **12**, 9-20.
51. G. Blasse and B. C. Grabmaier, *A General Introduction to Luminescent Materials*, Springer, Berlin, Heidelberg, 1994.
52. F. Wang, Y. Han, C. S. Lim, Y. Lu, J. Wang, J. Xu, H. Chen, C. Zhang, M. Hong and X. Liu, *Nature*, 2010, **463**, 1061-1065.
53. C. K. Rastogi, S. K. Sharma, A. Patel, G. Parthasarathy, R. G. S. Pala, J. Kumar and S. Sivakumar, *J. Phys. Chem. C*, 2017, **121**, 16501-16512.
54. P. Ghosh, A. Kar and A. Patra, *J. Appl. Phys.*, 2010, **108**, 113506.
55. R. Meltzer, S. Feofilov, B. Tissue and H. Yuan, *Phys. Rev. B*, 1999, **60**, R14012.
56. G. Mialon, S. Turkcan, A. Alexandrou, T. Gacoin and J.-P. Boilot, *J. Phys. Chem. C*, 2009, **113**, 18699-18706.
57. Z. Wang, T. Senden and A. Meijerink, *J. Phys. Chem. Lett.*, 2017, **8**, 5689−5694.
58. J. Zhou, A. I. Chizhik, S. Chu and D. Jin, *Nature*, 2020, **579**, 41-50.
59. F. Kim, S. Kwan, J. Akana and P. Yang, *J. Am. Chem. Soc.*, 2001, **123**, 4360-4361.